UNIVERSIDADE DE SÃO PAULO

INSTITUTO DE FÍSICA
CAIXA POSTAL 20516
01498-970 SÃO PAULO - SP
BRASIL

PUBLICAÇÕES

IFUSP/P-1010

FUSION AND PERIPHERAL PROCESSES IN THE $^{9}Be+^{10,11}B$ REACTIONS

L. Fante Jr., N. Added, R.M. Anjos, N. Carlin, M.M. Coimbra, M.C.S. Figueira, R. Matheus, E.M. Szanto and **A. Szanto de Toledo**
Instituto de Física, Universidade de São Paulo

To appear in Nuclear Physics A

Setembro/1992

FUSION AND PERIPHERAL PROCESSES IN THE $^{9}Be+^{10,11}B$ REACTIONS

L. Fante Jr., N. Added, R.M. Anjos, N. Carlin, M.M. Coimbra, M.C.S. Figueira, R. Matheus, E.M. Szanto and A. Szanto de Toledo

Instituto de Física da Universidade de São Paulo,Departamento de Física Nuclear, Laboratório Pelletron, Caixa Postal 20516 - 01498 São Paulo, SP - Brasil

ABSTRACT

Measurements of total fusion cross sections for $^{9}Be+^{10,11}B$ have been performed over the energy range from 2 to 4.5 times the Coulomb barrier. Elastic scattering and peripheral processes have also been investigated. No significant inhibition of the maximum fusion cross section is observed in spite of the low binding energy of the collision participants.

Nuclear reactions $^{10,11}B(^{9}Be,X)$, E = 10-40 MeV; measured $\sigma(\theta,E)$, $\sigma(A,Z)$ for fusion, quasi-elstic and elastic scattering, deduced critical and grazing angular momentum. Statistical model calculations. Identification of binary processes.

PACS numbers: 25.70.Jj; 25.70.Gh; 25.70.Lm

1. Introduction

Fusion studies involving light heavy-ion reactions have been intensively performed over the last few years in order to characterize the influence of the single particle structure of light s-d nuclei on the reaction dynamics[1,2]. Interesting systematic features were recently observed. The observed constant value[3] (σ_F^{max}1.0± 0.2 b) for the maximum fusion cross section for a very wide mass region, seems to show a tendency to decrease in the case of very light and weakly bound nuclei (see figure 1a). Experimental values for the fusion barrier height (V_B) and radius (R_B), when plotted as a function of the size of the system $\rho = (A_1^{1/3} + A_2^{1/3})$ display a discontinuity in the regular behaviour observed for the case of heavier systems ($\rho > 5$ fm)[2,4]. This behaviour, described in figure 1b, suggests that the specific structural characteristics of the light s-d nuclei have a strong influence on the prevailing reaction mechanisms. Furthermore some authors[5,6] claim that when very weakly bound nuclei are involved as in the case of ^{9}Be induced reactions, a behaviour different from other heavy ion reactions is observed, leading to very low fusion cross sections, when compared to the reaction cross section. In the case of the $^{9}Be+^{9}Be$ system[7], the fusion cross sections seem to reach very low values supposedly due to the strong competition with direct processes. In the case of $^{10,11}B+^{10,11}B$ reactions such a drastic effect is not observed[8]. For instance, the maximum fusion cross sections are still larger than $\sim$ 900 mb.

Large differential cross section are observed at backward angles in the elastic scattering of these very light nuclei[8–10]. The significant cluster spectroscopic factors and low separation energy seem to favour transfer processes as well as the formation of dinuclear configurations which may act as doorways to binary exit channels leading to strongly damped processes as observed[11,12] in the case of $^{10,11}B+^{10,11}B$, $^{16,17,18}O$.

In order to investigate the role of weakly bound nuclei in the reaction dynamics, which lead to a stronger competion between quasi-elastic and strongly damped processes, the $^{9}Be+^{10,11}B$ reactions have been studied at bombarding energies up to E/A $\sim$ 4 MeV. Data for elastic scattering, quasi-elastic, fusion and "non-fusion" processes were obtained.

A brief discussion of the experimental method is presented in section II. Results are indicated in section III. The discussions and conclusions are presented in section IV.

II. Experimental Procedure

The measurements were performed using ^{9}Be beams obtained from the University of São Paulo Pelletron accelerator. Molecular BeH^- and BeO^- primary beams were extracted from the ion source, with $\sim$ 400 enA intensity. The bombarding energies ranged from 10 MeV to 40 MeV. Self supporting ^{10}B and ^{11}B targets, 30 μgcm^{-2} to 50 μgcm^{-2} thick, were used. A very thin gold layer was deposited on the targets for normalization purposes.

Charged reaction products and evaporation residues were identified using a Position Sensitive Ionization Chamber (PSIC) followed by a large area solid state detector. The anode of the PSIC was composed of two complementary saw-bladed surfaces which supplied the position of the incident particle. Details on the experimental set up are given in reference 8.

Complete angular distributions were measured with the PSIC at E(^{9}Be) = 16 MeV, 27 MeV and 37 MeV in the range $3° \leq \theta_L \leq 43°$ in steps of 1°, along with excitation functions at 10 MeV $\leq$ E_L(^{9}Be) $\leq$ 40 MeV in steps of 1 and 2 MeV.

The same reactions, using reverse kinematics (i.e. ^{10,11}B beams on ^{9}Be target), were also exploited at the highest energy i.e. the compound nucleus is populated at the same excitation energy in an effort to identify the direct, strongly damped components and evaporation residues. In this case, the reaction products were simultaneously A and Z identified at a fixed angle $\theta_L = 16°$ using a time of flight (TOF) set up[8] , followed by an ionization chamber (IC).

Absolute cross sections were determined for the present study by comparing the elastic scattering cross sections with optical model predictions. The same procedure has been used to determine the amount of light contaminants (cargon and oxygen) in the target.

III. Experimental Results and Analysis

III.1. Elastic Scattering

The experimental angular distributions, presented in figure 2, were χ^2-fitted to optical model (OM) predictions. The computer code PTOLEMY[13] has been used for this purpose. The starting values for the OM parameters for the ^{9}Be+^{10,11}B, ^{9}Be+^{12}C and ^{9}Be+^{16}O were obtained from the literature[6-10]. Several sets of OM parameters were searched, i.e. energy independent and dependent ones (in the latter case a quadratic energy dependence for V and W has been searched). Details of the procedure used to extract OM parameters from the elastic scattering data have been outlined in reference 8. The fits are also presented in figures 2a and b and the OM parameters sets are listed in table 1.

It should be noted that only the data up to $\theta_{cm} \sim 60°$ were used in the fitting procedure due to the influence of processes like elastic transfer and compound elastic responsible for the enhancement of the back angle cross section.

To estimate the magnitude of the compound elastic (CE) cross sections, statistical model calculations were performed based on the code STATIS[14]. It is known that in such calculations the magnitude of the CE cross sections is sensitive to the values adopted for the level density parameters (LDP)[15]. Therefore in order to verify whether the CE process can be responsible for the back angle cross section, the LDP have been varied from A/8 to A/5. The results, shown in figure 3, suggest that the back angle cross section, at the highest energies, can be accounted for on the basis of the compound nucleus decay. In the measured angular region, the contribution of elastic-transfer processes is negligible. This process, as shown in reference 10, interferes significantly in very backward angles $\theta_{cm} \geq 150°$. Values for the total reaction cross section and grazing angular momenta were obtained from the complete angular distributions at E_L = 16 MeV, 27 MeV and 37 MeV (see table 1).

III.2. The Fusion Components

In the case of light heavy ion reactions the identification of evaporation residues (ER) becomes difficult due to the contribution of direct reaction products which may populate the same channels. In order to partly solve this ambiguity the reaction products energy spectra produced in a given reaction can be compared to the one produced in a reverse kinematics reaction leading to the same compound nucleus at the same excitation energy. In the case of nearly symmetric entrance channel, the ER spectra are similar in both cases due to the fact that the center of mass motions are similar in both cases (if desired, the influence of the center of mass (CM) motion can be removed by a simple change of reference frame converting energy spectra to Q-value spectra). Due to the anisotropy of the angular distribution of direct processes, the same does not happen with these direct components, associated to very different CM when detected in the laboratory at a given angle and originated by stripping (pick-up) or pick-up (stripping) processes in the direct (reverse kinematic) reaction at different CM angles. Consequently, in the latter case due to the anisotropy of the angular distributions, the products are formed with significantly different cross section. A further procedure to confirm the reaction mechanism can be provided by fits of the E.R. spectra to predictions of statistical model calculations. Typical spectra and unfolded contributions are also shown in figure 4 for several reaction products. The contribution of fusion and non fusion components are indicated. Details on the unfolding procedure are presented in reference 8, however it should be pointed out that, in this work, the E.R. time of flight spectra have been measured in the direct as well as reverse kinematic reactions, turning more consistent the data reduction procedure.

The presence of light contaminants in the B and Be targets has been determined quantitatively by the low energy elastic scattering data. In spite of observing a small amount of ^{12}C and ^{16}O contamination, their contribution in all the ER spectra has been subtracted based on Z and E distributions estimated by means of Monte-Carlo Hauser-Feshbach calculations (LILITA code)[16] and normalized to values for the ER cross sections found in the literature for the $^{10,11}B$+^{12}C[9,17] and ^{10,11}B+^{16}O reactions[18].

Values for differential cross sections were obtained for the ^{10,11}B+^{9}Be reaction as

well as ^{9}Be+^{10,11}B reaction at several angles, leading to similar values within the experimental uncertainties. The contribution of Z = 5 fusion components perturbed by the elastic tail in the B+Be channel and Z = 4 in the Be+B channel were cross checked with the data from the reverse kinematics reactions.

Angular distributions for individual elements are presented in figure 5 for the highest energy showing that the predictions of the statistical model, renormalized to the data, provide an overall satisfactory agreement. Total cross section for evaporation residues production as well as for complete fusion have been determined using the relation

$$\sigma_F(E) = \int_0^{\theta_{max}} 2\pi sin\theta_L \left\{ \sum_{Z=4}^{9} \left(\frac{d\sigma_Z}{d\Omega} \right) \right\} d\theta_L \qquad (3.1)$$

in which the experimental angular distributions were fitted by an analytical function[8] and extrapolated both to zero degree and beyond the largest measured angle. Thus the uncertainty in the total cross section, estimated to be $\sim$ 10% , takes into account counting statistics, extrapolation of the data to zero and large angles, uncertainties in the determination of the target thickness and detector solid angle and errors originated from subtraction of the contaminant spectra.

Excitation functions were measured at five angles θ_i, around the maximum value $(d\sigma/d\theta)_{max}$. Total cross sections were obtained from the relation

$$\sigma_T(E) = \int \left(\frac{d\sigma(E)}{d\theta} \right) d\theta \simeq R_i \left(\frac{d\sigma(E)}{d\theta_i} \right) \qquad (3.2)$$

where R_i values have been smoothly interpolated from values extracted from measured angular distributions. Z-distributions were obtained at some energies and compared to the predictions of the code LILITA[16] (see figure 6). A reasonable overall agreement has been achieved. Fits of the total fusion cross section to the Glas and Mosel model were used to determine the fusion barrier height (V_B) and radius (R_B) (see figure 7). The V_B and R_B values are listed in table 3. Experimental excitation functions for ^{9}Be+^{10,11}B confirm maximum values around 0.9barn which are comparable to the values measured for ^{10,11}B + ^{10,11}B systems or also, ^{10,11}B + ^{12,13}C[9,17] and still much larger than the 200 mb reported for the ^{9}Be+^{9}Be system[7]. In spite of dealing, in the Be+B reaction

with very weakly bound nuclei (i.e. the neutron separation energy is E_n = 1.67 MeV) the maximum fusion cross section is still comparable to the one observed for heavier systems[3], indicating that a drastic hindrance of the absolute value for fusion yield is not observed. However as indicated in figure 1 the values obtained for (V_B, R_B), which follow the general behaviour of neighbouring system suggest a relative inhibition of the fusion channel when compared to the expectation based on geometrical constraints and on the reaction cross section. Total reaction cross sections also indicated in figure 7 were obtained by optical model calculations based on fits of the elastic scattering data. The effect of the low binding energy of the ^{9}Be participant is observed in the fraction of the reaction cross section diverted to fusion reaching maximum values of $R = \frac{\sigma_F}{\sigma_R} \leq 0.6$ compared to 0.8 for the ^{10,11}B + ^{10,11}B and ^{10,11}B + ^{12,13}C systems[9,17].

The relative hindrance of the fusion probability of weakly bound nuclei is systematically discussed in reference 21.

The compound nucleus excitation energy dependence on the critical angular momentum, shown in figure 8 for both systems, indicate a behaviour similar to the one observed for the ^{10,11}B + ^{10,11}B systems[8] i.e., channels involving ^{10}B nuclei present an earlier deviation from the grazing trajectory. In a similar way, we observe that the compound nuclei $^{19(20)}$F are formed at high temperature ($T_{CN} \sim$ 2.5 MeV), superior to the critical temperature for fusion[3] $T_C \sim$ 1.47 MeV, leading to a consequent high level density ($\Gamma/D > 10^3$).

The fact that ^{9}Be+^{10}B fusion trajectory deviates earlier from the grazing trajectory, as in the ^{10}B+^{10}B case, reflects a higher entrance channel spin and may suggest that in these cases, the high angular momentum partial waves are feeding other processes than fusion such as break-up or strongly inelastic binary channels. In the first case the lower α-separation energy $S_\alpha(^{10}B)$ = 4.46 MeV compared to $S_\alpha(^{11}B)$ = 8.66 MeV may justify this behaviour which is consistent, as will be shown later, with the presence of larger α and Li yields observed in reactions involving ^{10}B.

III.3. The Non-Fusion Component Channels

It has been shown that besides the fusion and quasi-elastic channels, other non fusion channels are present in light heavy ion reactions[11,12]. These components, extracted according to the deconvolution of the energy (velocity) spectra described earlier and depicted in figure 4, present a binary character, as shown by the trajectory of the velocity vectors in the reaction plane indicated in figure 9.

The analysis of the direct and inverse kinematic spectra, confirm the presence of non-fusion processes and allow to estimate the anisotropy of the different yields as well as to determine their average Q-value (assuming a binary character of the channel). For this purpose, most probable values for the mass of the reaction product are estimated, based on the time of flight measurements.

Non-fusion components were clearly identified in the boron, carbon and nitrogen exit channels. The experimental Q-values for these channels are listed in table 3 together with their angle integrated cross sections. The anisotropy of the angular distributions, shown in figures 10a, b, seems to increase with the atomic number of the element and with bombarding energy suggesting that the mass transfer occurs via a direct process.

Discrete states are observed in the several mass spectra allowing the identification of the main process among all the energetically possible ones.

Assuming that these non-fusion components are originated by a binary process as suggested by the figure 9, their angular distributions can supply orbiting angles of analized within the framework of the Regge-pole model[22]

$$\frac{d\sigma}{d\Omega} = \frac{c}{sin\theta_{cm}} \left[exp\left(-\frac{\theta_{cm}}{\omega\tau}\right) + exp\left(-\frac{2\pi - \theta_{cm}}{\omega\tau}\right)\right]$$

This expression describes the decay of a rotating dinucleus with an angular velocity $\omega = \frac{\hbar\ell}{\mu R^2}$ where μ represents the reduced mass of the system, ℓ its angular momentum (which can be set equal to the grazing (ℓ_g) or critical (ℓ_c) angular momentum), and R represents the distance between the two centers of the dinucleus. Small values of

the "life angle" $\alpha = \omega\tau$ lead to forward peaked angular distributions associated with fast processes, whereas large α values, associated with large τ values when compared to the dinucleus rotation period T, are consequently associated with longer lived configurations and lead to more isotropic angular distributions. In this case the angular distribution tends to $\frac{d\sigma}{d\Omega} \alpha \frac{1}{sin\Theta}$.

The comparison between direct and reverse kinematics reactions has been performed at the highest energy at $\theta_{LAB} = 16°$. The energy spectra for fluorine an oxygen reaction products, converted to the C.M. reference frame become similar for both reactions ^{9}Be+$^{10(11)}$B as well as $^{10(11)}$B+^{9}Be, indicating that these elements correspond to evaporation residues. For these cases, the statistical model predictions fit satisfactorily the data.

In the case of nitrogen reaction products, the $Z = 7$ spectra from the reaction ^{9}Be+$^{10(11)}B$ are dominated by evaporation residues and are reproduced properly by the statistical model calculations. On the other hand, the $^{10(11)}$B+^{9}Be reactions seem to present an important non-fusion component. The fact that the $^{14(15)}$N elements are the most abundant indicates that the $Z = 7$ non-fusion products are essentially associated to direct α pick-up process leading to very anisotropic angular distributions. This is confirmed by the shape of the ^{9}Be (^{10}B, ^{14}N) spectrum. The ^{9}Be (^{11}B, ^{15}N reaction presents an overall cross section for this process three times larger than in the ^{10}B case. In both cases, the average excitation energy of the residual nucleus is $E^* \sim 10$ MeV.

Very small non-fusion contribution is observed in the production of carbon from the ^{9}Be+$^{10(11)}$B which are dominated by evaporation residues. Reactions on both isotopes present similar behaviour. A more significant yield is observed in the $^{10(11)}$B+^{9}Be channels, indicating an important anisotropy of the ^{9}Be ($^{10(11)}$B, C) channels. Although the ^{11}C (^{12}C) energy spectra present a clear sequence of peaks originated by proton pick-up processes, the production of ^{12}C (^{13}C) seems to be clearly dominant presenting important structures at low excitation energies. The fact that the simultaneous yield of the ^{7}Li and ^{8}Li partners is very low, supports the assumption that the mechanism is direct and strongly anisotropic.

The analysis of the boron spectra from the ^{9}Be ($^{10(11)}$B, B) reaction deserve a special treatment due to the presence of beam-like particles in the same way as the beryllium elements produced in the $^{10(11)}$B (^{9}Be, Be) reactions.

In the case of $Z = 5$ elements, a small contribution of evaporation residues is observed, of equal magnitude in both reactions, induced either by $^{10(11)}$B or ^{9}Be projectiles. Important direct components are also observed in all cases. The one neutron pick-up channels ^{9}Be ($^{10(11)}$B, $^{11(12)}$B)^{8}Be corresponding to the backward cross section for production of unstable ^{8}Be particles is clearly observed through transition to discrete boron states. This channel appears to be at most comparable in magnitude to the inelastic channel. Although clear transitions to discrete states are observed in the one neutron stripping channel i.e. ^{9}Be (^{10,11}B, ^{9,10}B) its intensity is not significant.

The inelastic transitions appear clearly also in the recoiling particle spectra i.e. ^{9}Be ($^{10(11)}$B, ^{9}Be)$^{10(11)}$B. Most of the transitions to discrete states can be associated to inelastic excitation of the $^{10(11)}$B projectile. The ratio between the production of $^{10(11)}$B inelastically scattered particles and ^{9}Be recoiling nuclei indicates a very anisotropic distribution with $\alpha \leq 40°$.

The production of lithium, in the ^{9}Be (^{11}B, Li) reaction is concentrated in ^{7}Li isotopes whereas in the case of ^{9}Be (^{10}B, Li) both ^{6}Li and ^{7}Li have similar abundance among them and much higher than in the ^{11}B case. The important anisotropy of the ^{9}Be (^{10}B, Li) reaction points toward the occurrence of a break-up process. On the other hand the ^{9}Be(^{11}B, Li) angular distribution appear to be quasi-isotropic (see figure 12).

IV. Conclusions

The ^{9}Be+^{10,11}B reactions have been investigated up to the energy E/A $\sim$ 5 MeV. Although it has been verified that the fusion process is dominant, important non statistical channels were identified. The elementar distributions of evaporation residues as well as their angular distributions are satisfactorily described by statistical model calculations. The $^{10(11)}B(^{9}Be,^{11(12)}B)^{8}$Be reaction does not appear to be dominant in spite of the low neutron binding energy in ^{9}Be. Furthermore no significant inhibition of the maximum fusion cross section is observed in comparison to the $^{10,11}B + ^{10,11}B$ reaction, but a systematic decrease of the importance of the fusion cross section in the total reaction cross section (σ_R) is verified when compared to the B+B systems (i.e. a decrease of σ_F/σ_R is observed).

The non-fusion channels present different "life angles" or orbiting angles leading to angular distribution with very different anisotropies. A weak correlation between amount of mass transfered and isotropy of the angular distribution is observed.

This work has been partly supported by the Conselho Nacional de Desenvolvimento Científico e Tecnológico (CNPq) and Fundação de Amparo à Pesquisa do Estado de São Paulo (FAPESP), Brasil.

REFERENCES

1) J.R. Birkelund, L.E. Tubbs, J.R. Huizenga, J.N. De and D. Sperber, *Phys. Reports* **56** (3), 107 (1979)

2) A. Szanto de Toledo, Proc. of XII Workshop on Nuclear Physics, Argentina (1989) - Ed. M.C. Cambiaggio, A.J. Kreiner and E. Ventura (World Scientific) p. 188.

3) O. Civitarese, B.V. Carlson, M.S. Hussein and A. Szanto de Toledo, *Phys. Lett.* **125B**, 22 (1983)

4) D.G. Kovar, D.F. Geesaman, T.H. Braid, Y. Eisen, W. Henning, T.R. Ophel, M. Paul, K.E. Rehm, S.J. Sanders, P. Sperr, S.L. Tabor, S. Vidgor and B. Zeidman, *Phys. Rev.* **C20**, 1305 (1979)

5) A.R. Omar, J.S. Eck, T.R. Ophel and J.R. Leigh, *Phys. Rev.* **C30** 1516 (1984) and *Phys. Rev.* **C37**, 1807 (1983)

6) M. Hugi, J. Lang, R. Müller, E. Ungricht, K. Bodek, L. Jarczyk, B. Kamys, A. Magiera, A. Strzalkowski and G. Willim, *Nucl. Phys.* **A368** 173 (1981) and L. Jarcyk, B. Kamys, A. Magiera, J. Sromicki, A. Strzalkowski, G. Willim, Z. Wrobel, D. Balzer, K. Bodek, M. Hugi, J. Lang, R. Müller and E. Ungricht, *Nucl. Phys.* **A369**, 191 (1981)

7) A.R. Omar, J.S. Eck, T.R. Ophel and J.R. Leigh, *Phys. Rev.* **C30**, 1516 (1984)

8) M.M. Coimbra, R.M. Anjos, N. Added, N. Carlin, L. Fante Jr., M.C.S. Figueira, G. Ramirez, E.M. Szanto and A. Szanto de Toledo, *Nucl. Phys.* **A535**, 161 (1991)

9) J.F. Mateja, A.D. Frawley, L.C. Dennis, K. Abdo and K.W. Kemper, *Phys. Rev.* **C25**, 2963 (1982) and J.F. Mateja, A.D. Frawley, D.G. Kovar, D. Henderson, H. Ikezoe, R.V.F. Janssens, G. Rosner, G.S.F. Stephens, B. Wilkins, K.T. Lesko and M.F. Vineyard *Phys. Rev.* **C31**, 867 (1985)

10) S. Albergo, S. Costa, R. Potenza, J. Romanski, C. Tuve, L. Jarczyk, B. Kamys, A. Magiera, A. Strazalkowski, R. Barna, V. D'Amico, D. De Pasquale and G. Mannino, *Phys. Rev.* **C43**, 2704 (1991)

11) A. Szanto de Toledo, M.M. Coimbra, N. Added, R.M. Anjos, N. Carlin Filho, L. Fante Jr., M.C.S. Figueira, V. Guimarães and E.M. Szanto, *Phys. Rev. Lett. 62*, **1255** (1989)

12) A. Szanto de Toledo, L. Fante Jr., R.M. Anjos, N. Added, M.M. Coimbra, M.C.S. Figueira, N. Carlin Filho, E.M. Szanto, M.S. Hussein and B.V. Carlson, *Phys. Rev.* **C42**, R815 (1990)

13) PTOLEMY - M.M. Macfarlane and S.C. Pieper - Argonne National Laboratory Report - ANL76 - 11 (unpublished).

14) STATIS - R.G. Stokstad, Yale University Wright Nuclear Structure Laboratory Report **52** (1972)

15) N. Carlin Filho, M.M. Coimbra, N. Added, R.M. Anjos, L. Fante Jr., M.C.S. Figueira, V. Guimarães, E.M. Szanto and A. Szanto de Toledo, *Phys. Rev.* **C40**, 91 (1989) and references therein.

16) LILITA, J. Gomez del Campo and R.G. Stokstad, ORNL, TM-7295 (unpublished).

17) J.F. Mateja, J. Garman and A.D. Frawley, *Phys. Rev.* **C28**, 1579 (1983) and J.F. Mateja, A.D. Frawley, R.A. Parker and K. Sartor, *Phys. Rev.* **C33**, 1307 (1986)

18) J. Gomez del Campo, J.A. Biggerstaff, R.A. Dayras, D. Shapira, A.H. Shell, P.H. Stelson and R.G. Stokstad, *Phys. Rev.* **C29**, 1722 (1984) and Y.D. Chan, D.E. di Gregorio, J.L.C. Ford Jr., J. Gomez del Campo, M.E. Ortiz and D. Shapira, *Phys. Rev.* **C25**, 1410 (1982) and references therein.

19) D. Glas and U. Mosel, *Phys. Rev.* **C10**, 2620 (1974) and *Nucl. Phys.* **A237**, 429 (1975)

20) P. Fröbrich, *Phys. Reports* **116** (6), 337 (1984)

21) M.C.S. Figueira, E.M. Szanto, A. Szanto de Toledo, M.P. Pato, M.S. Hussein and L.F. Canto - Preprint IFUSP/P-957 (1991) (to be published).

22) C.K. Gelbke et al., *Phys. Rep.* **42**, 311 (1978) and references therein.

FIGURE CAPTIONS

Fig. 1a: Experimental values (σ_F^{max}) for the maximum fusion cross section of the indicated systems. The lines represent the σ_F^{max} values predicted by the critical temperature model[3].

Fig. 1b: Experimental values for fusion barrier height ($V_B/Z_1Z_2e^2$) and radius (R_B). The dashed lines present fits to the data for $A_1^{1/3} + A_2^{1/3} > 5$ fm.

Fig. 2a: ^9Be+^{10}B elastic scattering angular distributions. The solid curves represent optical model fits to the forward angles data with the optical model parameter displayed in table 1.

Fig. 2b: ^9Be+^{11}B elastic scattering angular distributions. The solid curves represent optical model fits to the forward angles data with the optical model parameter displayed in table 1.

Fig. 3: ^9Be+^{10}B and ^9Be+^{11}B elastic scattering angular distributions at E_L = 37 MeV. The dotted curves represent the maximum possible compound elastic cross-section, wich, added to the forward angles fits (solid curves) generate the dashed curves.

Fig. 4: Experimental velocity spectrum deduced from the energy spectrum for the boron elements detected from the ^9Be+^{11}B reaction at $\theta_{lab} = 8°$. The solid line represents a smoothed velocity spectrum predicted by statistical model calculations (code LILITA)[16] for boron evaporation residues. The dashed line represents a fit to the spectrum resultant from the subtraction of the theoretical boron spectrum from the experimental velocity spectrum.

Fig. 5: Comparison between the experimental angular distributions for the several evaporation residues (closed circles) and the Monte Carlo Hauser-Feschbach calculations described in the text (histograms), for a) ^9Be+^{10}B reaction and b) ^9Be+^{11}B reaction. Full lines represent fits to the data - for details see the text.

Fig. 6: Experimental angle integrated evaporation residues cross-section (closed circles) for the ^9Be+^{10}B and ^9Be+^{11}B reaction compared to the statistical model (LILITA)[16] calculations (solid histogram).

Fig. 7: Experimental fusion cross-sections are plotted versus $1/E_{cm}$ for a) ^9Be+^{10}B and b) ^9Be+^{11}B systems. Dashed curves represent fits to the Glas and Mosel model and the dotted lines predictions based on the surface friction model[20]. The solid straight line represents the reaction cross-section predicted by the Optical Model using the parameter sets indicated in table 1.

Fig. 8: Excitation energy of the compound nucleus as a function of its critical angular momentum squared for ^{19}F (left) and ^{20}F (right). The full line represents the grazing $\ell_g(\ell_g + 1)$ trajectory obtained from fits to the elastic scattering data.

Fig. 9: Experimental average velocities for Z = 5, 6 and 7 for the non-fusion components (i.e. dashed component of figure 4). The semi-circles represent the expected trajectories for binary processes with indicated Q-values and for the expected average velocity of evaporation residues (dotted semi-circle).

Fig. 10: Angular distributions for non-fusion components a) for ^{9}Be+^{10}B and b) for ^{9}Be+^{11}B. Solid curves represent fits to expression 3.3. The value of α represents the "orbiting angle" of the system before decay.

TABLE CAPTIONS

Table 1: Optical model parameters used to fit the elastic scattering differential cross-sections, as well as total reactions cross-sections.

Table 2: Fusion barrier parameters obtained from fits of the evaporation residues cross-sections to te Glas and Mosel model.

Table 3: Experimental Q-values determined for the non-fusion components according to the assumed atomic mass for the residue.

	$^{9}Be + ^{10}B$		
E_{LAB}(MeV) / PARAM.	16	27	37
V_o (MeV)	61.78	61.78	61.78
W_o(MeV)	55.18	55.18	55.18
r_r (fm)	1.05	1.05	1.05
r_i (fm)	1.05	1.05	1.05
a_r(fm)	0.68	0.68	0.68
a_i (fm)	0.68	0.68	0.68
σ_{Rea}(mb)	1196	1418	1477
	$^{9}Be + ^{11}B$		
E_{LAB}(MeV) / PARAM.	16	27	37
V_o(MeV)	94.90	94.90	94.90
W_o(MeV)	71.12	71.12	71.12
r_r (fm)	1.08	1.08	1.08
r_i (fm)	1.08	1.08	1.08
a_r(fm)	0.59	0.59	0.59
a_i (fm)	0.59	0.59	0.59
σ_{Rea}(mb)	1197	1418	1478

Table 1

	R_B (fm)	V_B (MeV)
$^{9}Be + ^{10}B$	6.53 ± 0.13	4.65 ± 0.12
$^{9}Be + ^{11}B$	6.35 ± 0.13	4.69 ± 0.12

Table 2

$^{9}Be + ^{10}B$			
$^{10}B(^{9}Be, ^{A}B)^{(19-A)}Be$; Z = 5			
(A)	$(Q - VALVES)_{EXP}$ (MeV)		
	E_{LAB} = 16 MeV	E_{LAB} = 27 MeV	E_{LAB} = 37 MeV
9.0	-2.7 ± 0.4	-4.6 ± 0.7	-6.2 ± 0.9
10.0	-2.8 ± 0.4	-4.5 ± 0.7	-6.6 ± 1.0
10.5	-2.8 ± 0.4	-4.9 ± 0.7	-6.6 ± 1.0
11.0	-2.8 ± 0.4	-4.5 ± 0.7	-6.6 ± 1.0
12.0	-2.8 ± 0.4	-4.5 ± 0.7	-6.4 ± 1.0
13.0	-2.5 ± 0.4	-4.2 ± 0.6	-5.6 ± 0.8
$^{10}B(^{9}Be, ^{A}C)^{(19-A)}Li$; Z = 6			
(A)	$(Q-VALVES)_{EXP}$ (MeV)		
	E_{LAB} = 16 MeV	E_{LAB} = 27 MeV	E_{LAB} = 37 MeV
11	-2.8 ± 0.4	-4.6 ± 0.7	-6.7 ± 1.0
12	-2.6 ± 0.4	-4.6 ± 0.7	-6.8 ± 1.0
13	-2.4 ± 0.4	-4.5 ± 0.7	-6.3 ± 0.9
14	-2.0 ± 0.3	-3.8 ± 0.6	-5.7 ± 0.9

Table 3

$^{9}Be + {}^{11}B$			
$^{11}B\,(^{9}Be, {}^{A}B)^{(20-A)}Be$; Z=5			
(A)	$(Q - VALVES)_{EXP}$ (MeV)		
	E_{LAB} = 16 MeV	E_{LAB} = 27 MeV	E_{LAB} = 37 MeV
9.0	-2.5 ± 0.4	-6.3 ± 0.9	-7.6 ± 1.1
10.0	-2.5 ± 0.4	-6.6 ± 1.0	-7.9 ± 1.2
11.0	-2.4 ± 0.4	-6.6 ± 1.0	-8.1 ± 1.2
12.0	-2.5 ± 0.4	-6.7 ± 1.0	-8.1 ± 1.2
13.0	-2.3 ± 0.3	-6.6 ± 1.0	-7.9 ± 1.2
$^{11}B\,(^{9}Be, {}^{A}B)^{(20-A)}Li$; Z=6			
(A)	$(Q - VALVES)_{EXP}$ (MeV)		
	E_{LAB} = 16 MeV	E_{LAB} = 27 MeV	E_{LAB} = 37 MeV
11.0	-2.5 ± 0.4	-5.1 ± 0.8	-7.4 ± 1.1
12.0	-2.4 ± 0.4	-4.3 ± 0.8	-7.6 ± 1.1
13.0	-2.3 ± 0.3	-5.4 ± 0.8	-7.3 ± 1.1
14.0	-2.0 ± 0.3	-5.0 ± 0.8	-6.9 ± 1.0
$^{11}B\,(^{9}Be, {}^{A}N)^{(20-A)}He$ Z=7			
(A)	$(Q - VALVES)_{EXP}$ (MeV)		
	E_{LAB} = 16 MeV	E_{LAB} = 27 MeV	E_{LAB} = 37 MeV
13.0	—	-4.5 ± 0.7	-6.1 ± 0.9
14.0	—	-4.0 ± 0.6	-5.4 ± 0.8
14.5	—	-3.7 ± 0.6	-5.0 ± 0.8
15.0	—	-3.4 ± 0.5	-4.6 ± 0.7
16.0	—	-1.9 ± 0.3	-2.5 ± 0.4

Table 3
(Cont.)

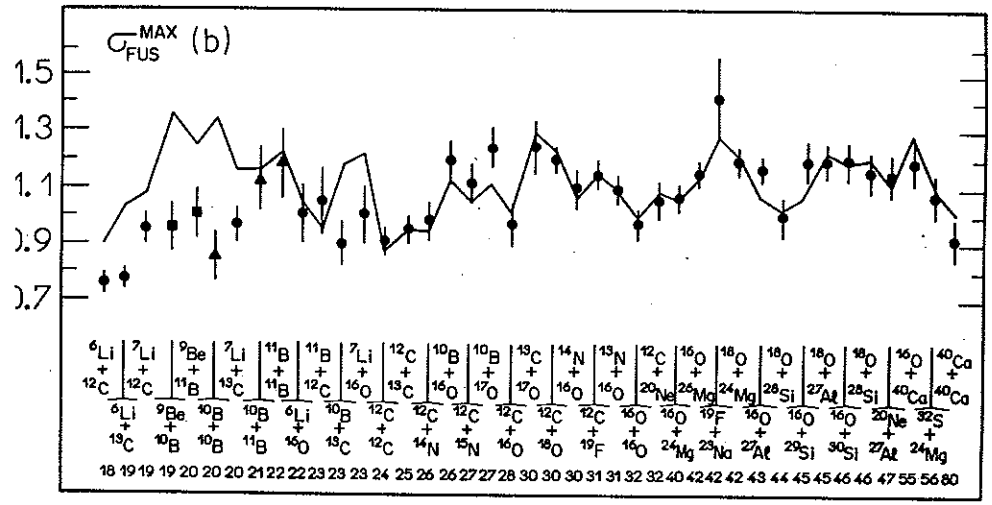

Fig. 1a

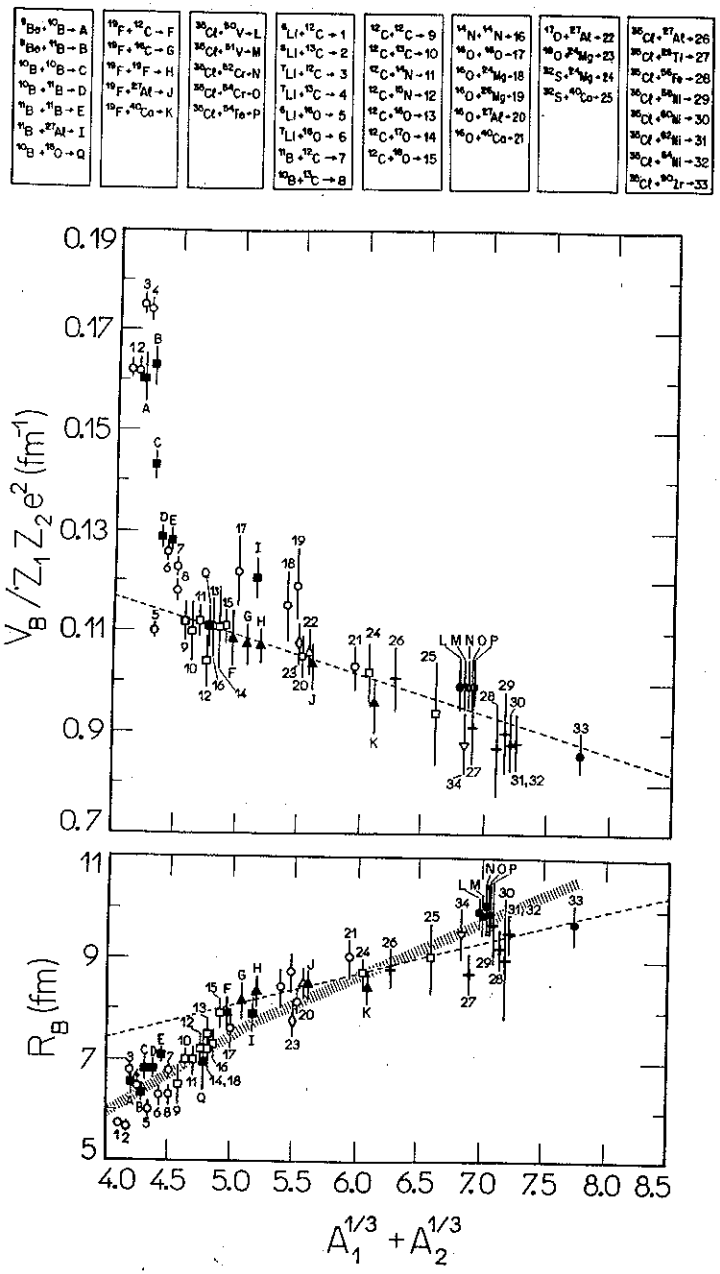

Fig. 1b

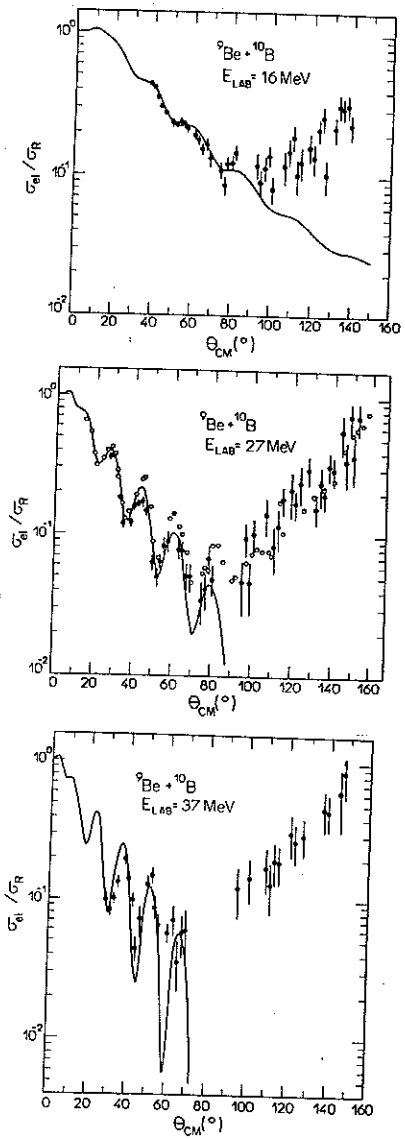

Fig. 2a

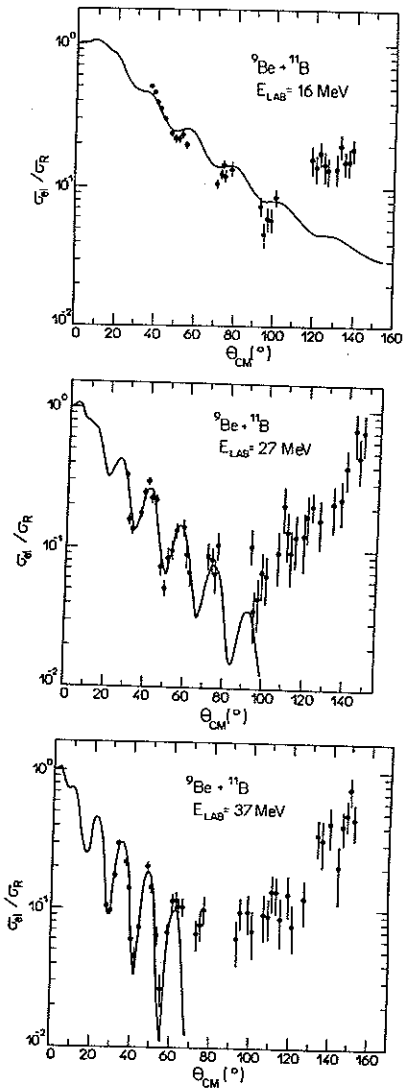

Fig. 2b

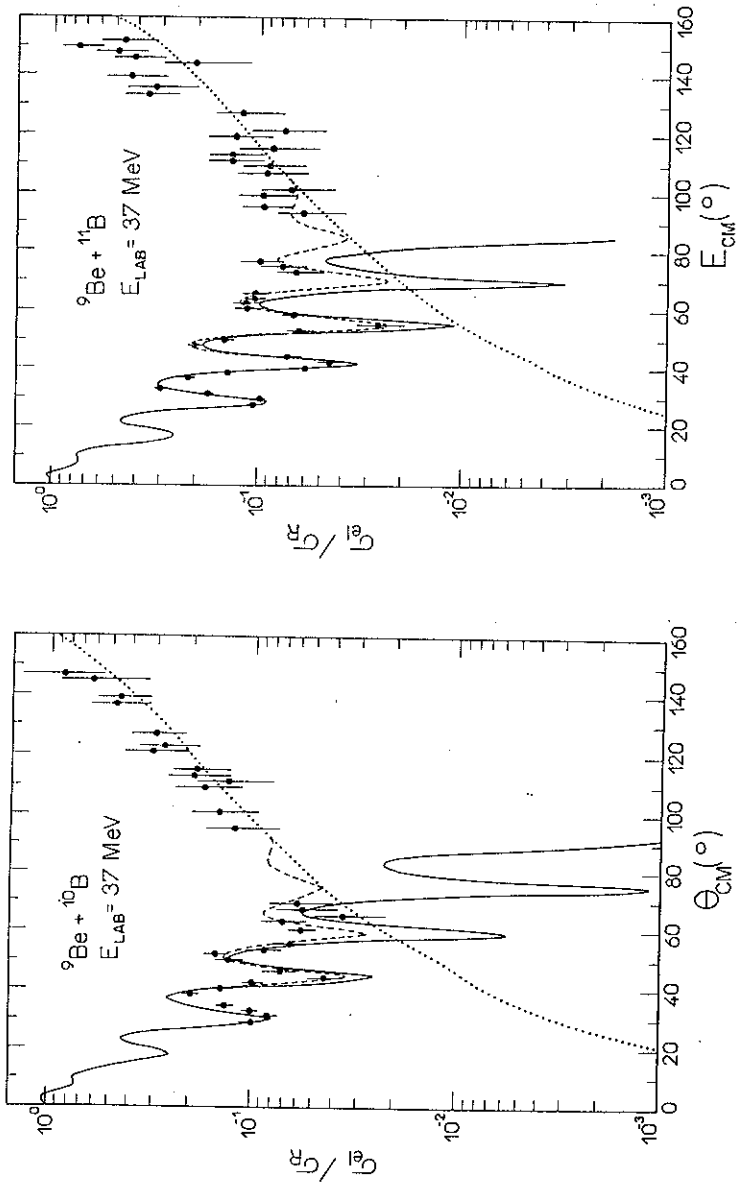

Fig. 3

$^{9}Be + ^{11}B$
$E_{LAB} = 37$ MeV

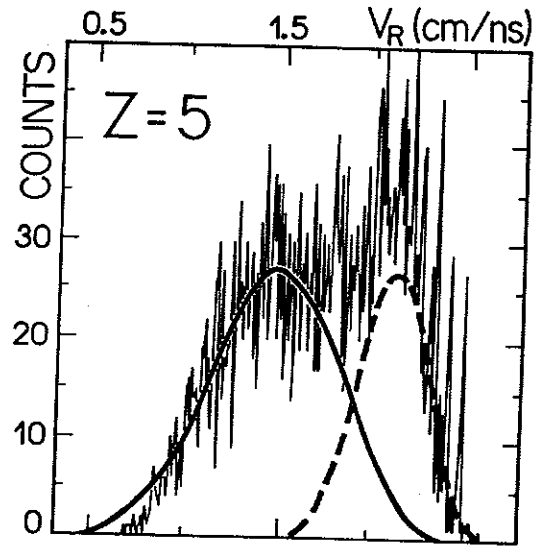

Fig. 4

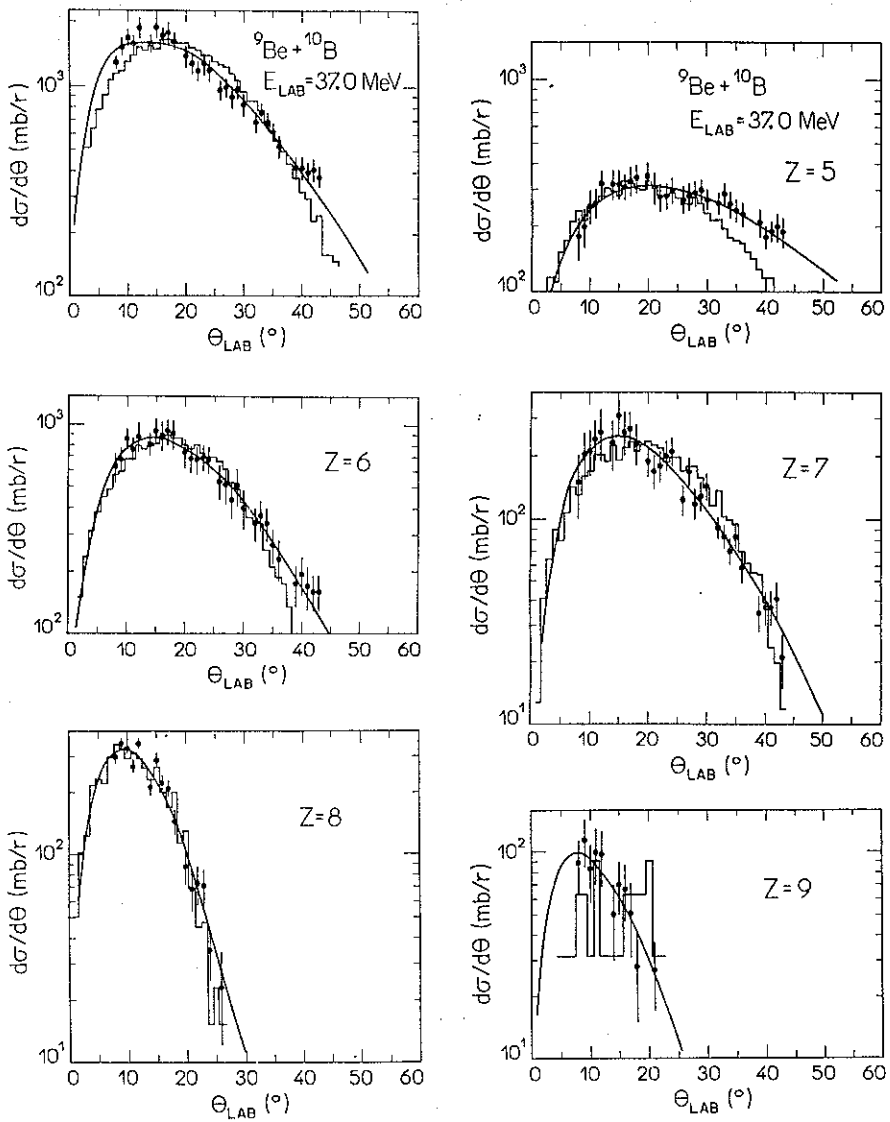
$^{9}Be + ^{10}B$
E_{LAB}=37.0 MeV
Z=5
Z=6
Z=7
Z=8
Z=9
dσ/dθ (mb/r)
θ_{LAB} (°)

Fig. 5a

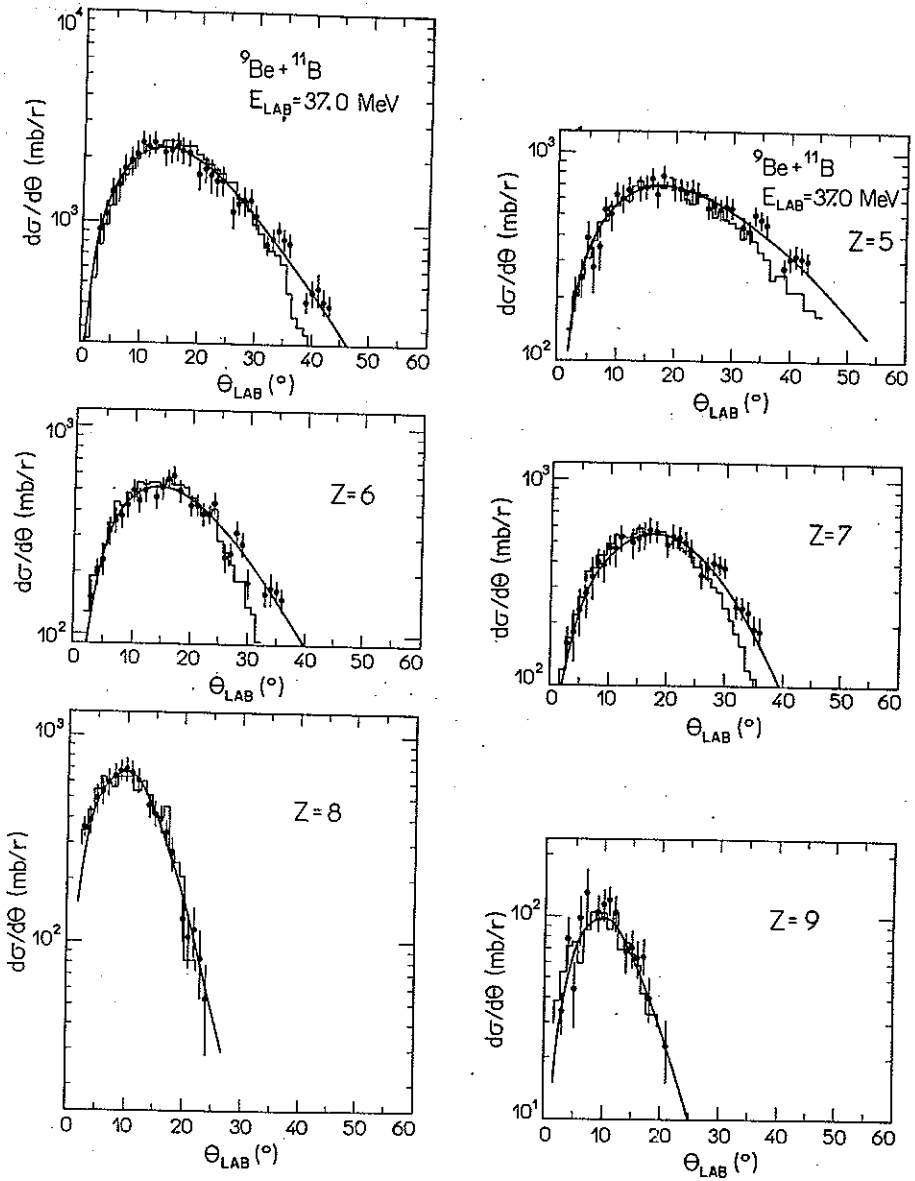
$^{9}Be + ^{11}B$
E_{LAB}=37.0 MeV
Z=5
Z=6
Z=7
Z=8
Z=9
dσ/dθ (mb/r)
θ_{LAB} (°)

Fig. 5b

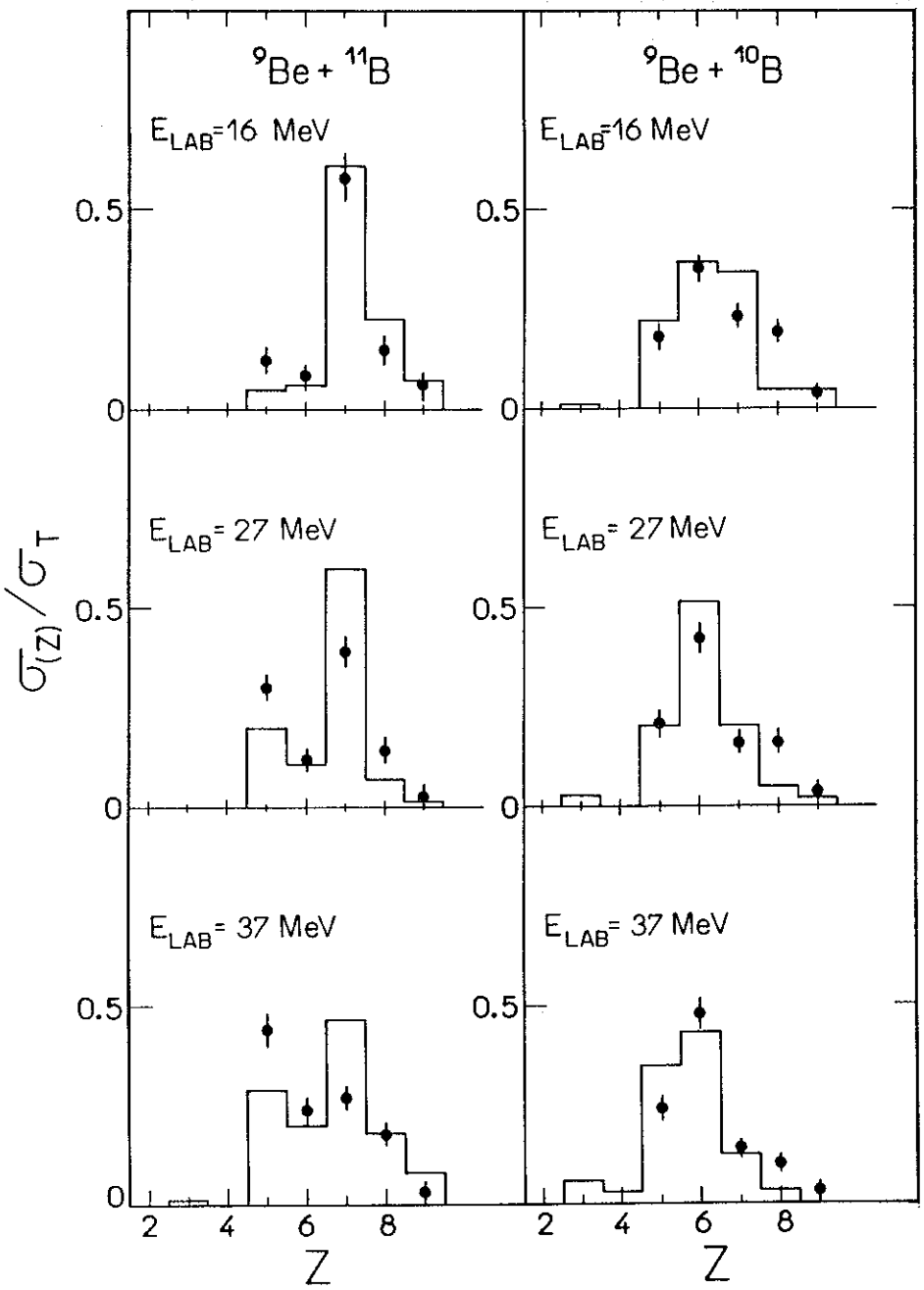

Fig. 6

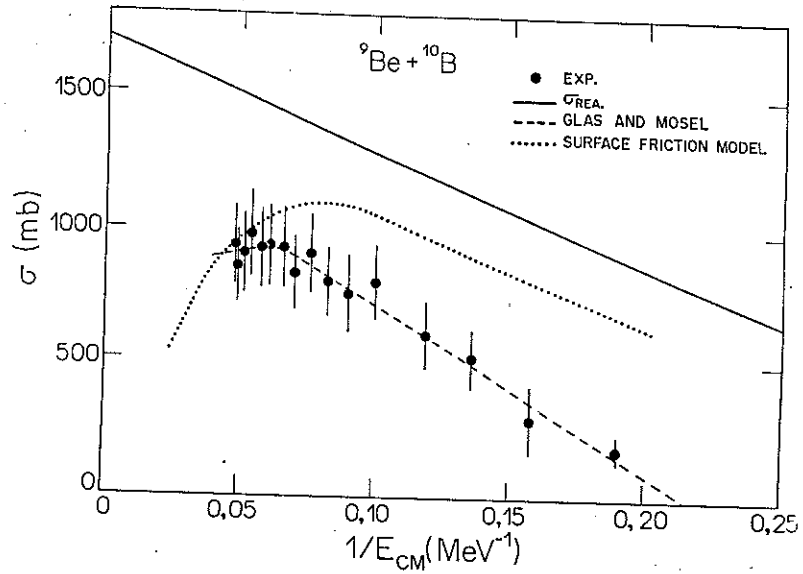

Fig. 7a

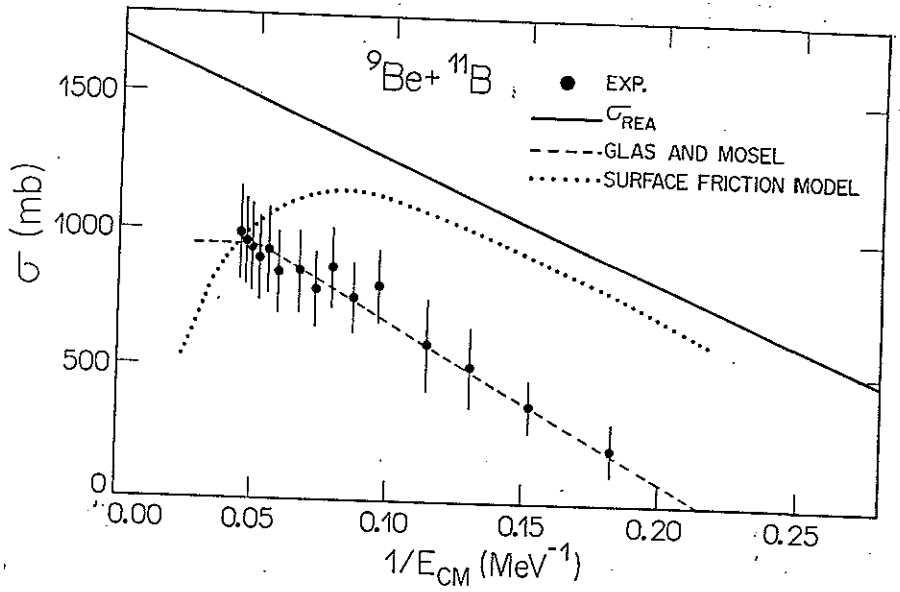

Fig. 7b

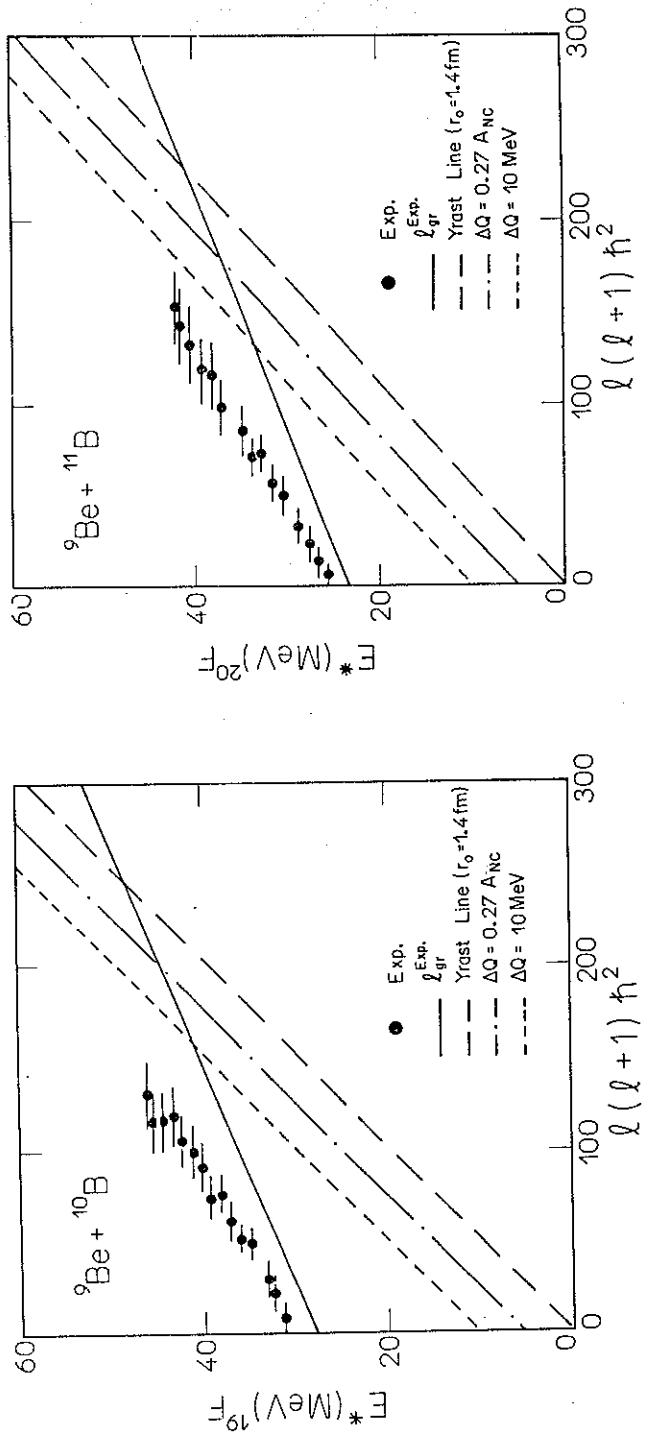

Fig. 8

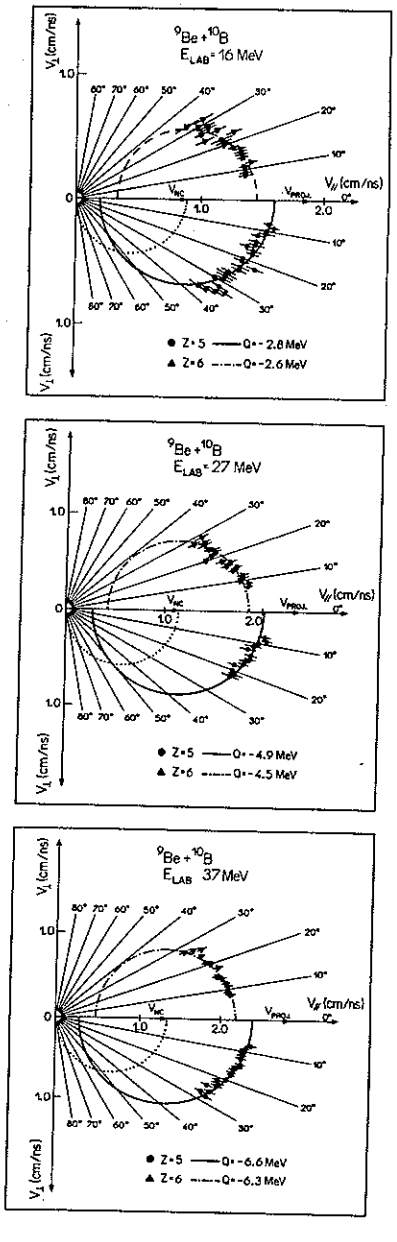

Fig. 9a

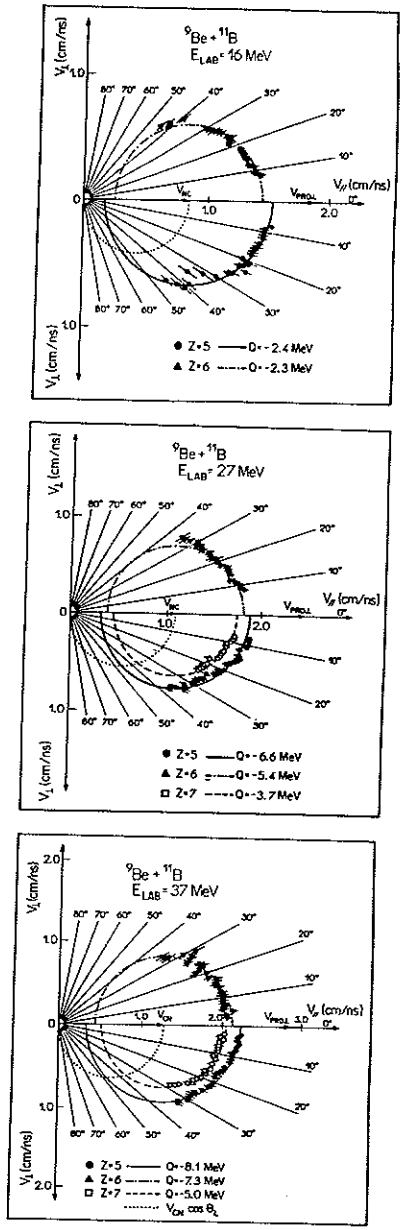

Fig. 9b

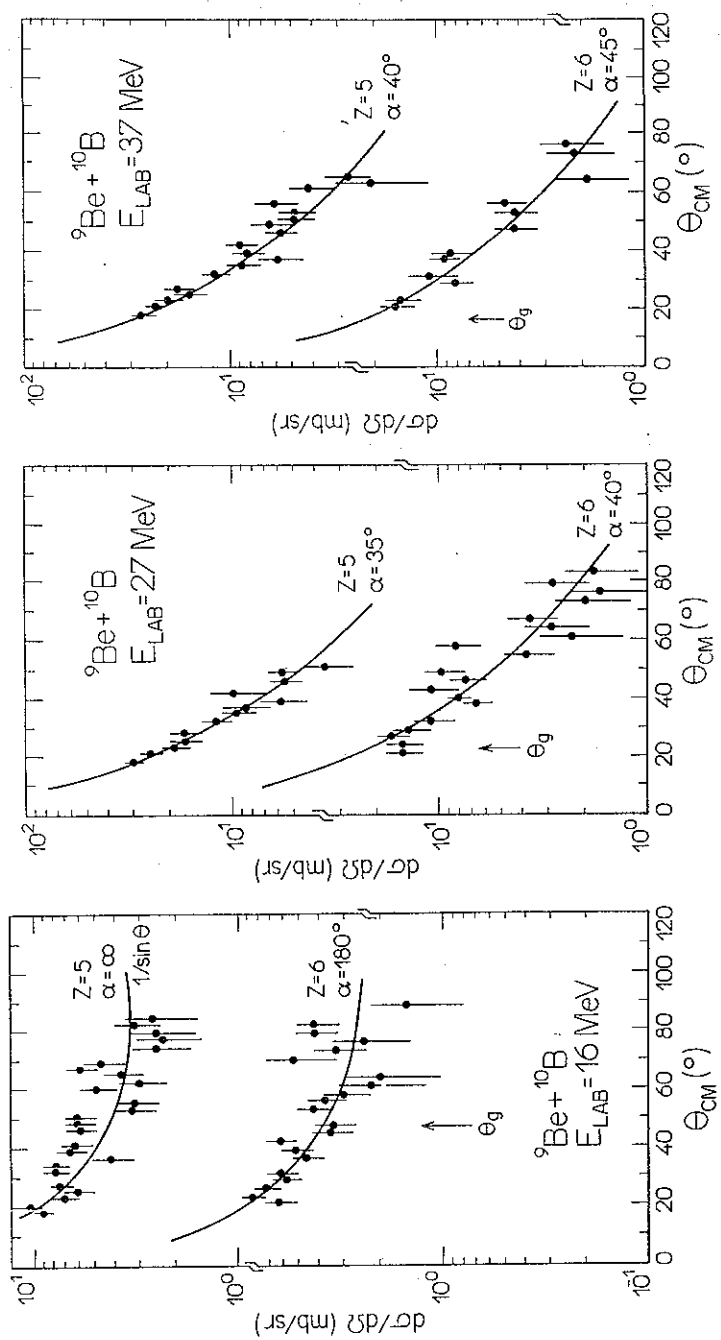

Fig. 10a

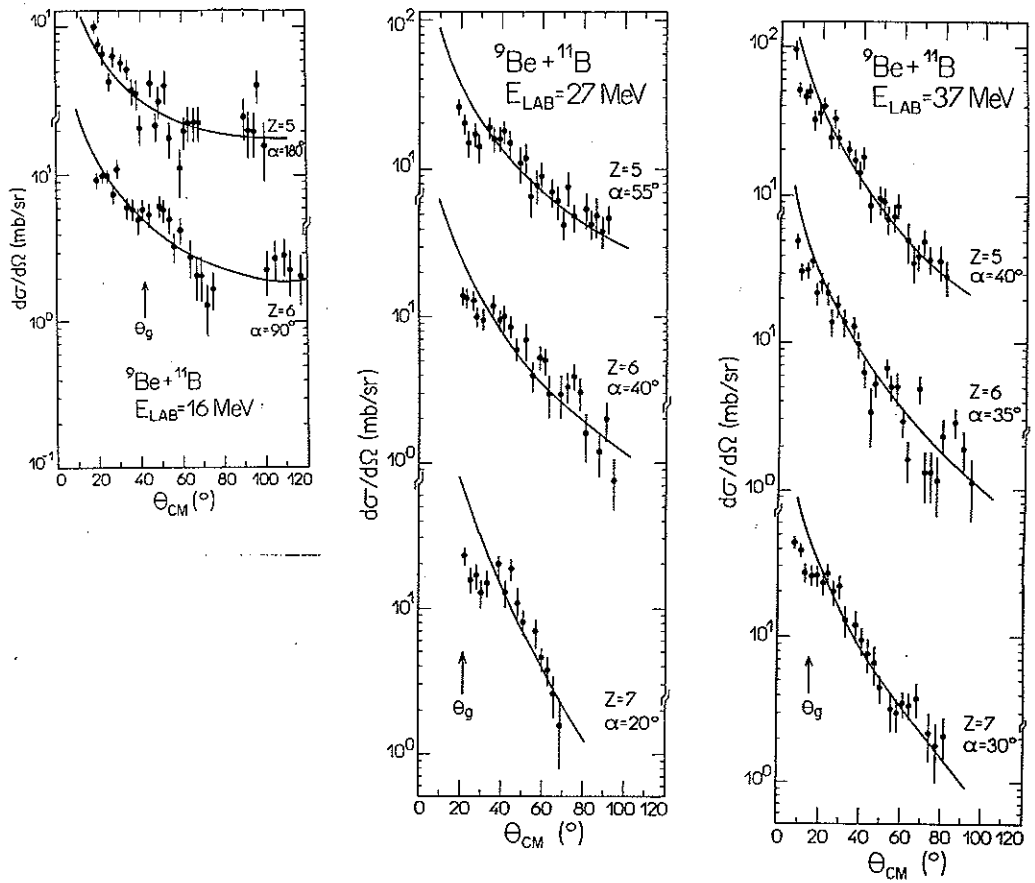

Fig. 10b